Interfacial Charge-Transfer Process on ZrO$_2$-TiO$_2$ Heterojunction and their Impact in the Photocatalytic Activity.

Diana Guerrero-Araque[a]*, David Ramírez-Ortega[a], Próspero Acevedo-Peña[b], Francisco Tzompantzi[a], Héctor Calderón-Benavides[c], Ricardo Gómez[a].

[a] *Universidad Autónoma Metropolitana, Departamento de Química. Av. San Rafael Atlixco 156, P.C. 09340. Mexico City, Mexico.*

[b] *Universidad Nacional Autónoma de México, Facultad de Química. Av. Universidad 3000, P.C. 04510. Mexico City, Mexico.*

[c] *ESFM-Instituto Politécnico Nacional, Av. Politécnico, Ed. 9 UPALM, México City, México.*

Abstract.

In this paper, ZrO$_2$-TiO$_2$ composites were synthesized by the sol-gel method with different ZrO$_2$:TiO$_2$ molar ratios (01:99, 05:95 and 10:90). The results identify two trends; at low ZrO$_2$ content is possible the incorporation of Zr^{4+} in the TiO$_2$ lattice provoking the generation of oxygen vacancies (1 mol % of ZrO$_2$); while to higher ZrO$_2$ content, ZrO$_2$-TiO$_2$ heterojunctions are created (5 and 10 mol % of ZrO$_2$). The photocatalytic activity was evaluated in the photodegradation of phenoxyacetic acid, 2,4-dichlorophenoxyacetic acid or 4-chlorophenol solutions. The ZT-5 composite show the best performance attributed to surface states in the interface of the ZrO$_2$-TiO$_2$ heterojunctions. This surface states act as traps for charge carriers favoring the spatial separation of the electron-hole pairs until to reach a maximum with the composite of 5 mol% of ZrO$_2$. The ZT-5 composite has the flat band more negative potential and the highest donor density indicating that these surface states are in optimal concentration. To higher ZrO$_2$ contents exists a less effective charge carriers separation that decreases the photocatalytic activity. Nevertheless, the molecule structure has an impact in the direct or indirect charge transfer process.

_____

*Corresponding Author Email: dianacga@msn.com

Introduction.

Titanium dioxide (TiO_2) is widely used as an effective photocatalyst for the degradation of organic pollutants, due to it is high chemical stability and efficiency, availability and low cost [1]. However, it is photocatalytic activity remains insufficient for practical applications since the high recombination rate of the photogenerated electron-hole pairs (e^--h^+) [2-3]. Thus, TiO_2 is coupled with others metal oxide such ZrO_2, CeO_2, NiO, WO_3 and Al_2O_3 to improve the photocatalytic activity [4-11].

In the same way, coupling of TiO_2 with ZrO_2 (2.8-5.1 eV) has attracted much attention in recent years [12- 18]. The increment in the photocatalytic activity in the TiO_2-ZrO_2 composites have been commonly associated to changes in their textural and structural properties such as high surface area, small particle size, high anatase phase content and energy band gap variation [19-21]. For example, Kokporka and co-workers reported the use of ZrO_2-TiO_2 composites in hydrogen production by photocatalytic water splitting, observing with a 5% of ZrO_2 content the best photocatalytic performance, which was attributed to the high specific surface area and phase composition [19].

On the other hand, the photoelectrochemical study can provide additional information related with the charge transfer process involved in the materials that can be associated with the photocatalytic activity. With this in mind, in the present paper pristine materials TiO_2, ZrO_2 and ZrO_2-TiO_2 composites with different ZrO_2:TiO_2 molar ratios (01:99, 05:95 and 10:90) were synthesized by the sol-gel method. The characterization of the materials was performed by XRD, nitrogen adsorption, diffuse reflectance UV-visible spectroscopy, Infrared spectroscopy, HR-TEM. Additionally, Electrochemical studies of the composite materials were carried out to understand the charge transfer process in the formed ZrO_2-TiO_2 heterojunction, and to get more information about the processes

involved in the photodegradation of phenoxyacetic acid (PAA), 2,4-dichlorophenoxyacetic acid (2,4 D) and 4-chlorophenol (4-CP), under UV-light.

2. Experimental.

2.1 Synthesis semiconductor materials.

Materials were obtained by means of sol-gel method. Pristine TiO_2 was prepared by mixing 1 mol of titanium *n*-butoxide, 16 mol of *n*-butanol and 0.5 ml of HNO_3 as the hydrolysis catalyst. The mixture was put under reflux at 353 K and 8 mol of deionized water were added to the reaction system. The system was maintained under reflux at 353 K during 16 h under constant stirring until gelling was achieved. Pristine ZrO_2 was synthesized in the same way using zirconium *n*-butoxide as zirconium precursor.

TiO_2–ZrO_2 composites were synthesized following the above described procedure. In this case, zirconium *n*-butoxide and titanium *n*-butoxide were mixed with the appropriate amount to obtain 1, 5 and 10 mol % of ZrO_2, this photocatalysts were labeled as ZT-1, ZT-5 and ZT-10, respectively. Finally, all the materials were dried at 353 K for 48 h and calcined at 773 K for 4 h in air.

2.2 Characterization.

XRD patterns were obtained with a Siemens D500 X-ray Diffractometer using CuKα radiation with $\lambda = 0.15418$ nm. The band gap energies were calculated by a McLean analysis of the electronic spectra obtained with a UV-visible spectrophotometer Perkin-Elmer Lambda 40, equipped with an integrating sphere and using MgO as reference. Surface areas were calculated by the BET method form the desorption branch of the nitrogen isotherm obtained with a Quantachrome Autosorb 3B instrument. High resolution transmission electron microscopy has been performed in the TEAM 05 microscope (NCEM-LBNL) in conditions of low dose rate in TEM mode. Experimentally 40 images are taken at different defocus settings and by using 80 kV as accelerating energy. The dose rate in all cases is 30 e$^-$/A^2 s in order to maintain the genuine atomic distribution of the heterojunctions. The treatment is completed by evaluating phase and amplitude images from an exit wave reconstruction procedure (MAcTempas ®) that uses the experimental

images at different defocus as limiting conditions. The phase image has precise information regarding atomic positions and atom nature of the observed columns in the sample.

2.3 Photocatalytic Activity.

The activities of the materials were evaluated at room temperature in the photodegradation of phenoxyacetic acid (PAA), 2,4-dichlorophenoxyacetic acid (2,4 D) or 4-chlorophenol (4-CP) solutions contained in 200 mL of water with an initial concentration of 2.6 x10^{-4} mol/L. The solutions were stirred in a home-made reactor for 30 min in dark to allow adsorption-desorption equilibrium of the contaminant on the solid. Afterwards, solutions were irradiated with UV light for 150 min using a Pen-Ray lamp of I=4.4 mW/cm^2. The photodegradation was monitored with a Cary 100 spectrophotometer by following the main absorption band as a function of the irradiation time, at 267 nm, 229 nm, 280 nm for PAA, 2,4-D, 4-CP, respectively. The Total Organic Carbon (TOC) concentration of the samples was measured using a TOC–V$_{CSN}$ analyzer Shimadzu. EIS measurement in the form of Nyquist plot was carried out in 30 min of exposure of a 0.03 M KClO$_4$ solution containing PAA, 4-CP and 2,4-D using the ZT-5 composite.

2.4 Preparation of films for electrochemical characterization.

0.2 g of pristine or composites and 0.1 g of polyethylene glycol (MW 20,000) were mixed in a mortar for 30 min to be perfectly homogenize, then 600 μL of acetic acid diluted with deionized water (0.2% v/v) were added drop-wise The mixture was homogenized to form a suspension and 200 μL were dispersed uniformly over a titanium plate with a pre-defined area. Finally, the film was dried for 24 h at room temperature and calcined at 623 K for 3 h [22-23].

2.4.1 Electrochemical Characterization

Electrochemical measurements were performed in a conventional three-electrode cell. A saturated electrode Ag/AgCl/3 M KCl was used as reference electrode [E$_{Ag/AgCl/3M}$ $_{KCl}$= 0.210 V/SHE]. The counter electrode was a graphite rod (99.9995% pure, Alfa Aesar) and previously prepared titanium plates were used as a working electrode. 0.03 M KClO$_4$ solution (supporting electrolyte) was prepared using Milli-pore water and KClO$_4$ with 97%

purity. Dissolved oxygen was removed from all solutions by bubbling nitrogen. The (photo) electrochemical tests were carried out in a conventional three-electrode cell equipped with a quartz window to allow the UV light illumination of the entire portion (1.23 cm^2) of the film exposed to the electrolyte. The 0.03 M KClO$_4$ solution (supporting electrolyte) to pH= 6 used for film characterization was prepared with Milli-pore water and KClO$_4$ (Baker Analyzed). Before each test, the electrolyte was bubbled with N$_2$ gas for 30 min. The illumination was performed using a Newport Q Housing (Model 60025) equipped with a 100 W Hg arc lamp. The semiconducting properties of the films were estimated from Mott-Schottky plots. The space charge capacitance of the film was potentiodynamically measured in the dark (v = 20 mVs^{-1}) at a frequency of 100 Hz with AC perturbation of ±10 mV (peak to peak) in a potential window with no faradaic currents measured. For the (photo) electrochemical measurements a GAMRY 1240 potentiostat was used.

3. Results and discussion.

3.1 Photocatalysts characterization.

XRD patterns of Pristine TiO$_2$ and ZT-x composites exhibit the characteristic diffraction peaks of anatase polymorph (JCPDS 84-1286), Figure 1. A small diffraction peak at a 2θ of 30.6° related to ZrO$_2$ tetragonal phase (JCPDS 79-1769) was observed on the ZT-10 composite, Figure 1- iv. In the other composites it cannot be observed due to the low ZrO$_2$ content and to the detection limit of the equipment employed for the measurement. The peak around 25.3° related to the (101) plane of the TiO$_2$ anatase phase diminishes in the presence of ZrO$_2$ evidencing a variation in the crystal size. This is associated to that the incorporation of ZrO$_2$ in the composites retards the crystallite grown and the crystallization process of the anatase [19, 24-26]. In contrast, the diffraction pattern measured for pristine ZrO$_2$ shows the presence of two different crystalline structures in the material: Tetragonal ZrO$_2$ (JCPDS 79-1769) and Monoclinic ZrO$_2$ (JCPDS 37-1484), Figure 1-v [27]. The crystallite size obtained from the diffraction patterns in Figure 1, it is summarized in Table 1. In addition the methodology here employed allowed to obtain ZrO$_2$ nanocrystals, see Table 1.

Furthermore, the Rietveld refinement was carried out on pristine TiO$_2$ and ZT-x composites diffraction patterns. Figure 2 shows that a and c parameters for pristine TiO$_2$

and ZT-x composites changes towards at higher values as the ZrO_2 content increase; these parameters accomplish a maximum for the ZT-5 composite, and maintain almost constant for ZT-10 composite. Based on these change, the increment in the lattice parameters in the ZT-1 composite can be related to the insertion of Zr^{4+} in the sol state by direct linking, favored from the synthesis method since the Zr^{4+} (ionic radius : 0.72 Å) is larger than Ti^{4+} (ionic radius: 0.605Å) [28-29]; while for ZT-5 and ZT-10 composites, part is in the TiO_2 lattice, and the rest as ZrO_2 forming a heterojunction (evidenced from TEM image for ZT-5 composite in Figure 5). This behavior might be related to generation of different defects in the composites.

The textural properties like specific surface area (S_{BET}), average pore diameter (d_{pore}) and pore volume (V_{pore}) of synthesized materials were measured by N_2 adsorption isotherms and are summarized in Table 1. By increasing the amount of ZrO_2 in composites, d_{pore} and V_{pore} increases. Furthermore, it is noteworthy that specific surface areas of ZT-x composites are greater than those measured for pristine TiO_2 and ZrO_2, thereby increasing the active sites for improvement of the photocatalytic performance.

Figure 3 shows the IR spectra of pristine TiO_2, ZrO_2, and ZT-x composites. The bands around at 1658 cm^{-1} and 3400 cm^{-1} correspond to OH groups and H_2O strongly adsorbed, respectively. For ZT-x composites (Figure 3 ii-iv) the band at 3400 cm^{-1} increase significantly, particularly for the ZT-5 composite, indicating the presence of a greater amount H_2O adsorbed, as most clearly seen in the inset in Fig. 3. (the inset shows the difference in transmittance when spectrum of pristine TiO_2 is subtracted). These species are considered favorable for the photocatalytic activity since a higher amount of radicals are expected to be formed during illumination [11, 30]. ZrO_2 spectra shows two bands at 3723 cm^{-1} and 3553 cm^{-1} attributed to the multi-centered OH groups bound to Zr^{4+} sites, Figure 3 v [31]. The band at 3634 cm^{-1} corresponds to Ti-OH and Zr-OH vibrations [11]. Pronounced band at 800 cm^{-1} in the pristine TiO_2 and ZT-x composites is assigned to the presence of Ti-O bonds [32]. The bands at wavenumbers of 563 cm^{-1} and 559 cm^{-1} are related to the vibrations of Ti-O-Ti and Zr-O-Zr bonds [33- 34].

The band gap (E_g) energy of the synthesized materials was estimated from the UV-vis diffuse reflectance measurements (Figure 4), using the Mclean analysis assuming

indirect allowed transitions [35-36]. The E_g values obtained of the materials are summarized in Table 1. The E_g value of pristine TiO_2 (3.1 e.V.) is less than the commonly reported of 3.20 e.V (Fig. 4a: i) [37]; which probably due to defects induced in the material during the synthesis. Moreover, pristine ZrO_2 exhibited three different transitions (Fig. 4b) at 2.8 (E_{g1}) and 3.7 eV (E_{g2}) and are related to the singly ionized states in the band gap, associated to oxygen vacancy defects (Fig. 4b: i-ii) [38]. The transition at 4.3 eV (E_{g3}) is related to interband transition (Fig. 4b: iii) [17]. The presence of different energetic transitions, ranging between E_{g1} and E_{g3}, are typical of materials having a large distribution of traps within the forbidden gap, phenomena widely reported for ZrO_2 oxides [39-42].

Increasing the amount of ZrO_2 in the ZT-x composites caused a displacement in E_g of the materials towards slightly higher values than that measured for pristine TiO_2 (Fig. 4.a ii-iv). This phenomenon is associated to the destruction of the lattice periodicity and the creation of defects [17]. However, E_g values obtained for ZT-x composites, showed no significant changes with regard to that found for TiO_2 (Table 1 and Fig. 4). This behavior shows that optical properties of ZT-x composites are determined by TiO_2, the material present in the highest proportion, and is characteristic of mixed oxides [43].

Figure 5 shows the phase image of the heterojunction in the ZT-x composites of the ZT-5 composite. The two involved phases (TiO_2 and ZrO_2) can be identified on the basis of their differences in lattice parameters. The phases TiO_2 (nanobar) and ZrO_2 (nanoparticles) are in an intimate contact at the separating interface indicating the formation of heterojunctions. The interplanar distances of 0.362 nm and 0.183 nm correspond to the lattice spacing of the ZrO_2 (100) plane and TiO_2 (200) plane, respectively. Interestingly Fig 5 shows a rather sharp interface where the different species in the projected columns of atoms can be directly related to the specific intensity of the atomic columns. Heavier atoms show higher intensities in phase images [44-45].

The interaction between ZrO_2 and TiO_2 can modify the properties of the ZT-x composites due to the formation of defects, which are involved in the separation of charge carriers during the photocatalytic reactions [43]. To obtain more information about the interface of the materials, the characterization of semiconducting properties of pristine and ZT-x composites was performed.

The semiconducting properties were evaluated from Mott-Shottky curves (C_{sc}^{-2} vs E) of synthesized materials (TiO$_2$, ZrO$_2$, ZT-1, ZT-5, ZT-10), previously supported on a Ti substrate. The capacitance of the space charge (C_{sc}) of materials, was estimated by potentiodynamic electrochemical impedance spectroscopy (EIS) in a potential window in which occur not charge transfer processes in the dark, in a 0.03 M solution KClO$_4$ (pH = 6.0). For this, a potential scan was performed from 1.5 V to -1.0 V at a rate of 20 mVs^{-1} at a frequency of 400 Hz [43]. Mott-Shottky curves are shown in Fig. 6. For all materials positive slopes in the region where the values of C_{sc}^{-2} vary linearly with the potential indicate that the evaluated materials exhibit type-n semiconductivity.

The flat band potential (E_{fb}) and donor density (N_d) were estimated from linear region in curves shown in Fig. 6, using the equation for Mott-Shottky for semiconductors type-n, equation (1) [46].

$$\frac{1}{C_{sc}^2} = \frac{2N_A}{N_d F \varepsilon_r \varepsilon_0}\left[E_m - E_{fb} - \frac{RT}{F}\right] \tag{1}$$

where N_A is the Avogadro's number (6.02 $\times 10^{23}$ mol^{-1}), N_d (cm^{-3}) is the density of donors, F is the Faraday constant ($\sim$9.65 $\times 10^4$ Cmol^{-1}), ε_r is the relative permittivity (86 and 24 for TiO$_2$ and ZrO$_2$, respectively) [19-20], ε_0 is the permittivity of vacuum (8.8542$\times 10^{-14}$ Fcm^{-1}), E_m (V) is the potential at which the measurement was carried out, E_{fb} (V) is the flatband potential, R is the gas constant (8.314 JK^{-1} mol^{-1}), and T is the absolute temperature ($\sim$ 298 K). The third term in the parentheses can be assumed to be negligible compared to the remaining three terms at room temperature.

The difference in relative permittivity of ZrO$_2$ and TiO$_2$ should affect the bulk dielectric properties of the ZT-x composites; therefore as a rough approximation, the permittivity of the composites may be considered as additive contribution of both oxides, then Eq. (2) is used for calculating the dielectric constant of the synthesized materials [47].

$$\varepsilon_{ZT-X} = \chi_{ZrO_2}\varepsilon_{ZrO_2} + \chi_{TiO_2}\varepsilon_{TiO_2} \tag{2}$$

where χ_i and ε_i are the volume fraction and the relative permittivity of each oxide.

The E_{fb} and N_d values estimated for pristine and ZT-x composites are shown in Table 2. The E_{fb} value obtained for TiO_2 (E_{fb} = -0.74 V) is near to the values commonly reported for TiO_2 in neutral pH [48]. In the case of ZrO_2, the E_{fb} obtained was -0.69 V, which is considerably less negative than the value expected for ZrO_2 (-1.58 V vs Ag/AgCl (KCl 3 M) [49]. Nonetheless, it is important mentioning that Mott-Schottky characterization of anodic ZrO_2 thin films showed a very similar behavior than reported for nanoparticulate film here characterized [50-51], and similar E_{fb} values were reported. The reason of this discrepancy between the expected and the measured value, could be related to the presence of different energetic states in the band gap of ZrO_2, as it was evidenced by the presence of three different transition from the Mclean analysis of reflectance spectra of this material, see Figure 4b.

For the ZT-x composites two different trends can be observed. At low Zr content in the composite, ZT-1, the E_{fb} is displaced toward a less negative value compared to that obtained for pristine TiO_2. This behavior might be related to generation of defects in TiO_2 lattice due to that at low ZrO_2 content the Zr^{4+} might being incorporated in the sol state. The incorporation of Zr^{4+} favors the generation of oxygen vacancies in the TiO_2 lattice inducing energetic states up bellow the conduction band [52 -54]. In contrast, at higher Zr content in the material, ZT-5 and ZT-10 composites, a displacement of E_{fb} towards more negative values is observed, as it has been reported in other studies with different composite materials ZrO_2/TiO_2, ZnO/TiO_2, WO_3/TiO_2 and $TiO_2/SrTiO_3$ [43, 55- 58]. As the ZrO_2 and TiO_2 were grown at the same time, it is expected that ZrO_2-TiO_2 grain boundaries are being generated in the composites forming ZrO_2-TiO_2 heterojunctions; the interface produces defects in the material that provokes the shift of E_{fb} in the TiO_2, and propitiate the charge carrier separation, impacting the photocatalytic performance of the composite [43]. It is worth mentioning that ZT-5 composite exhibits a maximum N_d, indicating a higher generation of energetic states in the heterojunction formed by the TiO_2 and ZrO_2 nanocrystals.

Another electrochemical method was employed to determine the conduction band position of the TiO_2 and ZT-x composites. It can be accessed the border of the conduction band position of the material by performing a cyclic voltammetry in the dark, and measuring the

onset for the cathodic current related to the filling of the empty energetic states in the conduction band of the oxide (Figure 6c.) [43]. The onset for the cathodic current is not altered when ZrO_2 is incorporated at 1 wt% (ZT-1 composite); however, for higher ZrO_2 content (ZT-5 and ZT-10 composites), the onset of the cathodic current is displaced towards more negative values. The flat-band potential measured from Mott-Schottky plots, present in Figure 6a and 6b., shows a similar trend. When only 1 %wt of ZrO_2 was incorporated, the E_{fb} was slightly displaced towards less negative values; however, at 5 and 10 wt% of ZrO_2 in the composites, the E_{fb} value measured for both materials is more negative than the E_{fb} measured for TiO_2. The changes in the on-set potential and the E_{fb} values are related to the dissimilar defects formed when the quantity of ZrO_2 added during the synthesis is altered.

In order to evaluate the charge carrier separation efficiency in the synthesized materials, current generation under illumination was measured imposing an anodic potential to propitiate the electrons transport towards the conducting substrate. Before the experiments, the electrolyte (0.03 M $KClO_4$, pH = 6) was bubbled with N_2 to avoid O_2 reduction in the semiconductor surface when illuminated. The results obtained for pristine and ZT-x composites are shown in Figure 7. First, the anodic bias was imposed during 60 s in order to stabilize the current in the dark, then the film was illuminated during other 60 s provoking an increase in the registered current, and after that light was again interrupted, causing a rapidly decrease in the currents to its value in the dark. These steps were repeated 5 times to evaluate the stability of the generated photocurrent. The low photocurrent values registered in the Figure 7 are due to the absence of an effective hole scavenger in the solution. For all materials an increase in the current was caused by illumination; however, the magnitude and the response was different for each material. The ZrO_2 film exhibited the lower photocurrent and rapidly decay with the number of perturbations. In contrast, photocurrent registered with TiO_2 films continuously increase with the number of perturbation, but its response with time while illuminated was sluggish, reflecting the presence of traps that difficult the transport of electrons towards the rear contact [59]. On the other side, ZT-x composites exhibited a behavior totally different that base materials: at low Zr content in the composite, ZT-1, the photocurrent was small but stable with the number of perturbation, and at higher Zr content, ZT-5 and ZT-10 composites, the response

to illumination was fast reaching higher currents that pristine TiO_2, but rapidly decrease with time and number of perturbations. The different behavior in the performance of the materials is evidencing defects with different nature in the composites as a function of the Zr content. Additionally, the material with the superior performance was the ZT-5 composite, since it has the highest electron-hole separation and the best transport of electrons propitiated by the TiO_2-ZrO_2 heterojunction. Nonetheless, it is worth pointing out that a higher photocurrent could not be strictly associated to a more efficient performance during photocatalysis, because other processes, such charge carrier transport. These are taking place in the films during photocurrent measurement; while simultaneous oxidation and reduction reactions take place in the composite agglomerates during photocatalysis.

3.2 Evaluation of photocatalytic activity.

The synthesized materials and Evonic P_{25} were evaluated in the photocatalytic degradation of three different contaminants commonly found in pesticides: phenoxyacetic acid (PAA), 2,4-dichlorophenoxyacetic acid (2,4-D) and 4-chlorophenol (4-CP). In a typical experiment, 100 mg of photocatalyst was dispersed in 200 mL of a solution containing ~13 mmol of pollutant (pH = 6). The suspension was kept under magnetic stirring during the whole experiment with air bubbling. Prior to illumination, the suspension was kept in the dark during 30 mins to allow the adsorption of the pollutant onto the photocatalyst surface. The variation of pollutant concentration was followed by UV-vis at different wavelengths (x nm for PAA, x nm for 2,4-D and x nm for 4-CP). The change of pollutant concentration with time employing the synthesized materials is shown in Fig. 7, for the first 150 min of UV irradiation. Pristine ZrO_2 exhibited the worst photocatalytic activity. On the other hand, ZT-x composites exhibited superior photocatalytic activity that their base materials, Fig. 7a, indicating that the incorporation of ZrO_2 during the synthesis avoid recombination by improving the charge carrier separation in the material, as it has been reported for other TiO_2 based composited oxides [43,60-63]. Furthermore, ZT-5 composite has a higher activity than Evonic P_{25}.

The experimental data were fitted to a pseudo zero-order kinetic (Figures 7a-ii, 7b-ii and 7c-ii), indicating that reaction rate is independent of the concentration of pollutant in the solution [64]. The kinetic parameters obtained are summarized in Table 3. Despite the

nature of the pollutant, the ZT-5 composite exhibited the best performance in all cases, confirming the results obtained from the photocurrent measurements in Figure 6. The three pollutants are adsorbed onto the photocatalyst surface, however, the higher rate was observed for the PAA because to that it can be adsorb more strongly than the others compounds. This is associated to that the chlorine atom in the others molecules leads the desorption of organic compounds. Also, the higher PAA adsorption increases the probability of the oxidation through the holes or surface hydroxyl radicals. Furthermore, the chloride anion competes with organic species for the active sites and lowers the reaction rate [65-66]. Also, the kinetic constants of the other composites are also higher that their base materials; however, their behavior was dependent of the nature of pollutant. While ZT-1 composite exhibited higher kinetic constant for PAA degradation, ZT-10 composite showed a better performance in the degradation of 2,4-D and 4-CP. This is probably associated to that at low ZrO_2 content, the Zr^{4+} incorporation provokes a separation center that may positively influence the mobility of photogenerated charge carriers so that more holes can reach the surface trapping sites [53,67]. On the other hand, at higher Zr content, the excited electrons will have stronger power to reduce oxygen leading to the efficient formation of superoxide radicals favoring the production of hydroxyl radicals [69].

The total organic carbon (TOC) removal efficiency was measured to evaluate the performance during photocatalytic oxidation using pristine TiO_2, ZrO_2 and ZT-x composites. The results confirm the same behavior followed by UV-vis suggesting that the pollutants also had been mineralized efficiently under UV light irradiation (Figure 9) [70]. Additionally, for the ZT-5 composite the TOC removal efficiency is the 92.7, 75 and 92.1% for PAA, 2,4-D and 4-CP, respectively.

Two electrochemical techniques were employed to discern if degradation of pollutants follows a direct charge transfer mechanism (through holes) or an indirect mechanism (through radical species); employing the film made with ZT-5 composite, as it showed the best performance (Fig. 8 and 9). Linear voltammetry under manually shopped light were measured in absence and in presence of each pollutant (0.2632 mM), in a 0.03 M $KClO_4$ (pH = 6) electrolyte, previously bubbled with N_2. The potential scan was performed from the open circuit potential measured under illumination in the anodic direction. The

obtained I vs E curves are shown in Figure 10. The presence of 4-CP and 2,4-D do not affected the photocurrent measured, indicating that its degradation follows an indirect pathway [71]. In contrast, PAA considerably increases the photocurrent measured, indicating that direct charge transfer at photocatalyst interface is taking place during its degradation.

Electrochemical impedance spectroscopy (EIS) was also employed to verify the observed behavior in the linear voltammetries. A particular advantage of this technique is that films do not need to be biased, so the measurement is carried out at the potential induced by illumination. Furthermore, if an oxidant, such oxygen, is present in the electrolyte, oxidation and reduction reactions will take place over the semiconductor surface, like in photocatalysis, representing a more realistic approximation to the process occurring during the photocatalytic degradation of pollutants. Nevertheless, it is worth mentioning that this experiment only provides an estimation of the initial rate for the charge-transfer process at the surface of the photocatalyst, and that transport phenomena of the pollutant to the photocatalyst surface in the suspension is not considered. The EIS spectra (Nyquist diagrams) measured in air bubbled electrolyte in presence and absence of pollutants are shown in Fig. 11. In all cases one semicircle is observed, indicating that only the charge transfer reaction resistance in parallel with a capacitance related to the double layer is involved in the observed response. The Nyquist spectra in Figure 11 were fitted to a $R_S(R_{CT}C_{dl})$ electric equivalent circuit using the software Zplot, where: R_S stand for the resistance of the solution, R_{CT} stand for the charge transfer resistance and C_{dl} stand for the double layer capacitance. It is worth mentioning that in all cases a $\chi^2 \sim 10^{-4}$ was obtained during fitting the EIS spectra experimentally obtained. The results obtained from fitting are summarized in Table 4.

Although the EIS spectra obtained in the dark is not displayed in Fig. 11, the parameters obtained from fitting are shown in Table 4. In absence of pollutant, the illumination carried to a considerable decrement of the charge transfer resistance, as expected [72-73], and an increase in the double layer capacitance probably due to increment of ions in the double layer formed in the semiconductor/electrolyte interface. The time constant, τ, resulting from the product of C_{dl} and R_{ct}, is inversely proportional to the

velocity of the process taking place in the interface at the time of the measurement [65]. The addition of the pollutants to the electrolyte provoked in all cases a decrease in R_{CT} and τ. It is worth pointing out that τ exhibits an inverse order that the kinetic constant in Table 3, indicating its direct correlation to photocatalytic process. The values of R_{CT} (Table 4) increase and k (Table 3) decrease with increasing the number of chlorine substituents in the aromatic ring of the pollutant, suggesting that the presence of Cl^- difficult the interaction of the pollutant with the radical formed during photocatalytic. Additionally, τ values obtained for 4-CP and 2,4-D are very near to the obtained for water oxidation (without pollutant), confirming that the degradation of these pollutant take place by an indirect pathway. Instead, τ value for PAA is two times lower that those obtained for the other pollutants and water oxidation, indicating that direct charge transfer process is happening during its photocatalytic degradation.

Generally, a higher photocatalytic performance is associated with a high specific surface area, small particle size, and small band gap (E_g) energy [60-62]. Nevertheless, in this case, no significant changes were observed in the specific surface area of the ZT-x composites and the energy band gap of ZT-x composites do not follow the trend of degradation (Table 1). Otherwise, the characterization of the semiconducting properties of ZT-x composites indicated two different trends (Table 2). For the ZT-5 composite (the material with the best performance) the defects induced energy states that favor the spatial separation of the photogenerated charge carries increasing the photocatalytic performance of the composites, as it is illustrated in Scheme 1, with a maximum concentration (N_d, Table 2). Based on the characterization of the materials, the incorporation of ZrO_2 at low quantities (1% in weight in the present study), provokes the creation of defects changing the E_{fb} of the materials towards less negative values, indicating the formation of deep energy states below the conduction band. These states might trap the photogenerated electrons and transfer them to the oxygen in the solution, increasing the performance of the material. On the other hand, when the ZrO_2 is present art higher quantities, the shifting the E_{fb} towards more negative values indicates the formation of semiconductor heterojunctions as it has been previously reported [43,55-58]. The displacement of E_{fb} have been associated to the generation of energetic states in the interface of the oxides [43], causing an upward band bending of the oxides in contact. These states formed in the interface might trap

photogenerated electrons, avoiding its recombination with photogenerated holes, and considering the ionized states in the ZrO_2, electron might be transported through them to react with oxygen in the solution. The differences in the behavior of ZT-5 and ZT-10 composites are associated to a less effective charge carriers separation at the interface of the heterojunction when the ZrO_2 content is increased, as it have been reported for other TiO_2-based composites [41, 43]. Finally, it is worth mentioning that ZT-1 composite was more efficient than ZT-10 composite to degraded PAA, while ZT-10 composite degraded more efficiently the 4-CP and 2,4-D than ZT-1 composite. The change in the trend could be related to the different species generated during photocatalytic reaction, as PAA is degraded by direct charge transfer and, 4-CP and 2,4-D by and indirect pathway (Figure 9).

4. Conclusions.

Pristine TiO_2, ZrO_2 and ZrO_2-TiO_2 composites with different ZrO_2:TiO_2 molar ratios (01:99, 05:95 and 10:90) were synthesized by sol-gel method. The incorporation of ZrO_2 into TiO_2 provokes dissimilar defects according to the ZrO_2 content. The photocatalytic activity of the synthesized materials was evaluated in the degradation of phenoxyacetic acid (PAA), 2,4-dichlorophenoxyacetic acid (2,4 D) or 4-chlorophenol (4-CP) under UV-light observing to increase until reaching a concentration of 5 mol% of ZrO_2. The behavior can be associated with the formation of energy states that retard the recombination of electron hole pair. These states can act as trap the photogenerated electrons and transfer them to the oxygen in the solution, increasing the performance of the material. The results suggest that the phenoxyacetic acid (PAA) is degraded by direct charge transfer and 2,4-dichlorophenoxyacetic acid (2,4 D) and 4-chlorophenol (4-CP), and indirect pathway.

Acknowledgements

References

[1] I.K. Konstantinou, T.A. Albanis, Appl. Catal. B Environ. 49 (2004) 1–14.

[2] M.R. Hoffmann, S.T. Martin, W. Choi, D.W. Bahnemann, Chem. Rev. 95 (1995) 69-96.

[3] R. Daghrir, P. Drogui, D. Robert, Ind. Eng. Chem. Res. 52 (2013) 3581-3599.

[4] V. Keller, F. Garin, Catal. Commun. 4 (2003) 377–383.

[5] X. Lin, J. Xing, W. Wang, Z. Shan, F. Xu, F. Huang, J. Phys. Chem. C. 111 (2007) 18288-18293.

[6] B. Sun, G. Zhou, T. Gao, H. Zhang, H. Yu, Appl. Surf. Sci. 364 (2016) 322–331.

[7] T. Cao, Y. Li, C. Wang, L. Wei, C. Shao, Y. Liu, J. Sol-Gel Sci. Technol. 55 (2010) 105–110.

[8] I.A. de Castro, J.A. de Oliveira, E.C. Paris, T.R. Giraldi, C. Ribeiro, Ceram. Int. 41 (2015) 3502–3510.

[9] A.A. Ismail, I. Abdelfattah, M. F. Atitar, L. Robben, H. Bouzid, S.A. Al-Sayari, D.W. Bahnemann, Sep. Purif. Technol. 145 (2015) 147–153.

[10] Q. Luo, Q.-Z. Cai, X.-W. Li, Z.-H. Pan, Y.-J. Li, X.-D. Chen, Q-S, Yan, Trans. Nonferrous. Met. Soc. China 23 (2013) 2945−2950.

[11] H. Zou, Y.S. Lin, Appl. Catal. A. Gen. 265 (2004) 35–42.

[12] S.N. Basahel, T.T. Ali, M. Mokhtar, K. Narasimharao, Nanoscale Res. Lett. 10 (2015) 1-13.

[13] V. Vishwanathan, H.-S. Roh, J.-W. Kim, K.-W. Jun, Catal. Lett. 96 (2004) 23-28.

[14] K.V.R. Chary, G.V. Sagar, D. Naresh, K.K. Seela, B. Sridhar, J. Phys. Chem. B. 109 (2005) 9437-9444.

[15] H.R. Chauke, P. Murovhi, P.E. Ngoepe, N.H. de Leeuw, R. Grau-Crespo, J. Phys. Chem. C. 114 (2010) 15403-15409.

[16] R.A. Lucky, Y. Medina-Gonzalez, P.A. Charpentier, Langmuir 26 (2010) 19014-19021.

[17] A. Emeline, G.V. Kataeva, A.S. Litke, A.V. Rudakova, V.K. Ryabchuk, N. Serpone, Langmuir 14 (1998) 5011-5022.

[18] D. Ciuparu, A. Ensuque, G. Shafeev, F. Bozon-Verduraz, J. Mater. Sci. Lett. 19 (2000) 931-933

[19] L. Kokporka, S. Onsuratoom, T. Puangpetch, S. Chavadej, Mater. Sci. Semicond. Process. 16 (2013) 667–678.

[20] X. Qu, D. Xie, L. Cao, F. Du, Ceram. Int. 40 (2014) 12647–12653.

[21] B. Neppolian, Q. Wang, H. Yamashita, H. Choi, Appl. Catal. A. Gen. 333 (2007) 264–271.

[22] H. Xu, X. Tao, D.-T. Wang, Y.-Z. Zheng, J.-F. Chen, Electrochim. Acta 55 (2010) 2280-2285.

[23] X. Li, D.-T. Wang, J.-F. Chen, X. Tao, Electrochim. Acta 80 (2012) 126-132.

[24] S-M. Chang, R-A. Doong, J. Phys. Chem. B 110 (2006) 20808-20814.

[25] W. Zhou, K. Liu, H. Fu, K. Pan, L. Zhang, L. Wang, C-C. Sun. Nanotechnology 19 (3) (2008) 035610.

[26] M. Fan, S. Hu, B. Ren, J. Wang, X. Jing. Powder Technol. 235 (2103) 27-32.

[27] S. Bajpai, S. Singh, V. Srivastava, RSC Adv. 5 (2015) 28163-28170.

[28] P.E.R. Blanchard, S. Liu, B.J. Kennedy, C.D. Ling, Z. Zhang, M. Avdeev, L-Y. Jang, F. Lee, C-W. Pao, J-L. Chen, Dalton Trans. 43 (2014) 17358–17365.

[29] S. Huang, Y. Yu, Y. Yan, J. Yuan, S. Yin, Y. Cao, RSC Adv. 6 (2016) 29950–29957.

[30] Z. Ding, G.Q. Lu , P.F. Greenfield, J. Phys. Chem. B. 104 (2000) 4815- 4820.

[31] E. Escalona Platero, M. Pefiarroya Mentruit, Catal. Lett. 30 (1995) 31-39.

[32] D.C. Leite Vasconcelos, V. Conceição Costa, E.H. Martins Nunes, A.C. Soares Sabioni, M. Gasparon, W. Luiz Vasconcelos, M. S. A. 2 (2011) 1375-1382.

[33] A.N. Murashkevich, A.S. Lavitskaya, T.I. Barannikova, I.M. ZharskiiJ, Appl. Spectrosc. 75 (2008) 1-5.

[34] Y. Hao, J. Li, X. Yang, X. Wang, L. Lu, Mater. Sci. Eng. A 367 (2004) 243–247.

[35] D. Reyes-Coronado, G. Rodríguez-Gattorno, M.E. Espinosa-Pesqueira, C. Cab, R. de Coss, G. Oskam, Nanotechnology 19 (14) (2008) 145605.

[36] S.-M. Chang, R.-A. Doong, Chem. Mater. 19 (2007) 4804-4810.

[37] K.M. Reddy, S.V. Manorama, A.R. Reddy, Mater. Chem. Phys. 78 (2002) 239–245.

[38] Z. Wang, B. Yang, Z. Fu, W. Dong, Y.Yang, W. Liu, Appl. Phys. A 81 (2005) 691-694.

[39] F. Di Quarto, S. Piazza, C. Sunseri, M. Yang, S.-M. Cai, Electrochim. Acta 41 (1996) 2511-2522.

[40] Y.-J. Lin, J.-F. Yu, J. Non. Cryst. Solids 426 (2015) 132–136.

[41] S. Verma, P. Kar, A. Das, D.K. Palit, H.N. Ghosh. J. Phys. Chem. C 112 (2008) 2918-2926.

[42] P. Maity, T. Debnath, A. Akbar, S. Verma, H.N. Ghosh, J. Phys. Chem. C 117 (2013) 17531−17539.

[43] D. Ramírez-Ortega, A.M. Meléndez, P. Acevedo-Peña, I. González, R. Arroyo, Electrochim. Acta 140 (2014) 541–549.

[44] K. Miyazawa, J. Yano, I. Honma, M. Akaishi, J. Am. Ceram. Soc. 83 (2000) 2315–2317.

[45] X. Wang, J.C. Yu, C. Ho, A.C. Mak, Chem. Commun. (2005) 2262–2264.

[46] R. Beranek, Adv. Phys. Chem. 2011 (2011) 1-20.

[47] B.S. Narwade, P.G. Gawali, R. Pande, G.M. Kalamse, J. Chem. Sci. 117 (2005) 673-676.

[48] M. Morozova, P. Kluson, J. Krysa, M. Zlamal, O. Solcova, S. Kment, T. Steck, J. Sol-Gel Sci. Technol. 52 (2009) 398–407.

[49] Y. Xu, M.A.A. Schoonen, Am. Mineral. 85 (2000) 543-556.

[50] V.D. Jović, B.M. Jović, Corr. Sci. 50 (2008) 3063-3069.

[51] V.D. Jović, B.M. Jović, J. Electrochem. Soc. 155 (2008) C183-C188.

[52] T. López, F. Rojas, R. Alexander-Katz, F. Galindo, A. Balankin, A. Buljan, J. Solid State Chem. 177 (2004) 1873–1885.

[53] P. Goswami, J.N. Ganguli, Dalton Trans. 42 (2013) 14480-14490.

[54] C. Di Valentin, G. Pacchioni, A.Selloni , J. Phys. Chem. C 113 (2009) 20543–20552.

[55] R. Bendoni, E. Mercadelli, N. Sangiorgi, A. Strini, A. Sangiorgi, A. Sanson, Ceram. Int. 41 (2015) 9899-9909.

[56] N. Smirnova, Y. Gnatyuk, A. Eremenko, G. Kolbasov, V. Vorobetz, I. Kolbasova, Olga Linyucheva, Int. J. Photoenergy 2006 (2006) 1-6.

[57] J. Zhang, J.H. Bang, C. Tang, P.V. Kamat, ACS Nano 4 (2010) 387-395.

[58] W. Smith, A. Wolcott, R.C. Fitzmorris, J.Z. Zhang, Y. Zhao, J. Mater. Chem. 21 (2011) 10792-10800.

[59] P. Acevedo-Peña, G. Vázquez, D. Laverde, J.E. Pedraza-Rosasa, J. Manríquez, I. González, J. Electrochem. Soc. 156 (2009) C377-C386

[60] G. Yang, Z. Yan, T. Xiao, Appl. Surf. Sci. 258 (202) 8704-8712.

[61] S. Bai, H. Liu, J. Sun, Y. Tian, S. Chen, J. Song, R. Luo, D. Li, A. Chen, C.-C. Liu, Appl. Surf. Sci. 338 (2015) 61-68.

[62] M. Li, X. Li, G. Jiang, G. He, Ceram. Int. 41 (2015) 5749-5757.

[63] J.C. Tristao, F. Magalhaes, P. Corio, M.T.C. Sansiviero, J. Photoch Photobio. A. 181 (2006) 152-157.

[64] L. Li, W. Zhu, P. Zhang, Z. Chen, W. Han. Water Res. 37 (2003) 3646-3651.

[65] A. Piscopo, D. Robert, J.V. Weber, Appl. Catal. B Environ. 35 (2001) 117–124.

[66] D. Robert, A. Piscopo, J.V. Weber, Sol. Energy 77 (2004) 553–558.

[67] J. Lukác, M. Klementová, P. Bezdicka , S. Bakardjieva, J. Subrt, L. Szatmary, Z. Bastl, J. Jirkovsky, Appl. Catal. B Environ. 74 (2007) 83–91.

[68] B. Gao, T.M. Lim, D.P. Subagio, T-T. Lim, Appl. Catal. A. Gen. 375 (2010) 107–115.

[69] L.C. Lei, Y. Zhang, X.W. Zhang, Y.X. Du, Q.Z. Dai, S. Han, Ind. Eng. Chem. Res. 46 (2007) 5469-5477.

[70] C. Anderson, A.J. Bard, J. Phys. Chem. B 101 (1997) 2611-2616.

[71] R. Vedarajan, S. Ikeda, N. Matsumi, Nanoscale Res. Lett. 9 (2014) 1-5.

[72] W. Ke, G. Fang, J. Wang, P. Qin, H. Tao, H. Lei, Q. Liu, X. Dai, X. Zhao, Appl. Mater. Interfaces 6 (2014) 15959-15965.

Graphical abstract

Heterojunction ZrO$_2$-TiO$_2$ 5 %

Defects induced in the interface

CB

e$^-$

e$^-$

Ionized states

CB
E$_{FB}$

e$^-$

e$^-$

TiO$_2$

3.1 eV

4.3 eV

ZrO$_2$

3.7 eV

2.8 eV

VB

h$^+$

h$^+$

h$^+$

h$^+$

h$^+$

VB

h$^+$

h$^+$

Direct charge transfer

Indirect charge transfer

OH*

Phenoxyacetic acid
Degradation 98%

4-Chlorophenol
Degradation 98%

2, 4 Dichlorophenoxyacetic acid
Degradation 82%
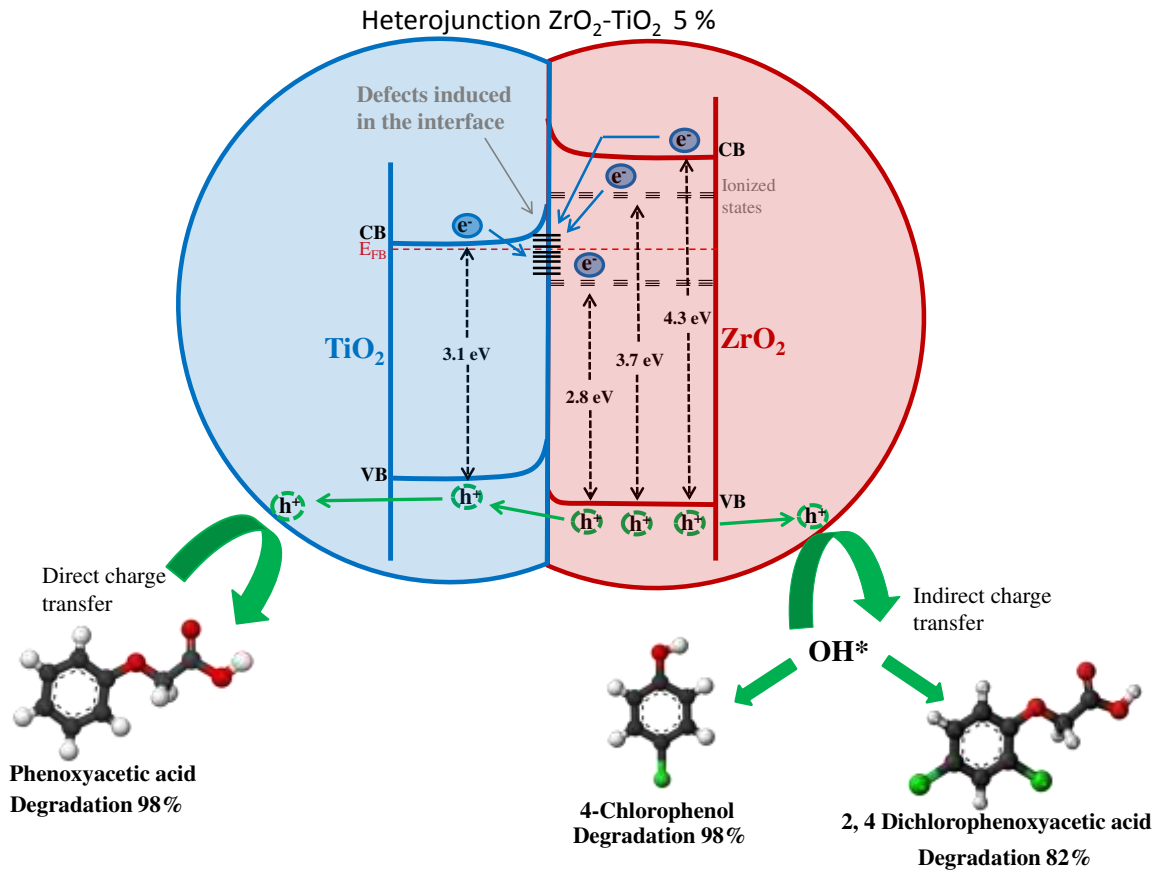
Figure Captions.

Fig. 1. a) XRD patterns obtained of the synthesized materials: i) TiO_2, ii) ZT-1, iii) ZT-5, iv) ZT-10 and v) ZrO_2.

Fig. 2. The a and c lattice parameters of pristine TiO_2 and the ZT-*x* composites obtained by Rietveld refinement.

Fig. 3. FTIR spectra of the synthesized materials: i) TiO_2, ii) ZT-1, iii) ZT-5, iv) ZT-10 and v) ZrO_2.

Fig. 4. Shematic presentation of the Mclean analysis of the adsorption edge for determining the energy band gap E_g of a): i) TiO_2, ii) ZT-1, iii) ZT-6, iv) ZT-10 and b) Shematic presentation of the Mclean analysis of the adsorption edge for determining the energy band gap E_g of ZrO_2: i) 2.8 eV, ii) 3.7 eV and iii) 4.3 eV.

Fig. 5. TEM characterization of the heterojunction in the ZT-5 composite.

Fig. 6. a) Mott-Shottky plots of: i) TiO_2, ii) ZrO_2 and b) Mott-Shottky plots of ZT-*x* composites with different content of ZrO_2 : i) ZT-1, ii) ZT-5 and iii) ZT-10). The C_{sc} were obatianed at 400 Hz in 0.03 M $KClO_4$ (pH = 6.0) aqueous solution. c) Cyclic voltammetry of pristine TiO_2 and the ZT-*x* composites.

Fig. 7. Photocurrent response under UV light on-off process at applied voltage of 0.5 V (vs Ag/AgCl) measured employing films made with the different photocatalyst here synthesized: i) TiO_2, ii) ZrO_2, iii) ZT-1, iv) ZT-5 and v) ZT-10.

Fig. 8. a. Variation of concentration with time for the different pollutants: i) PAA, ii) 2,4-D and iii) 4-CP, employing the synthesized materials. Photocatalyst concentration 0.5 g/L and initial pollutant concentration 0.2632 mM. b. Pseudozero order kinetics: i) PAA, ii) 2,4-D and iii) 4-CP.

Fig. 9. The TOC removal of PAA, 4-CP and 2,4-D with pristine TiO_2, ZrO_2 and ZT-*x* composites.

Fig. 10. Linear voltammetry under shopped UV light measured for the film made with the ZT-5 composite in different electrolytes: i) $KClO_4$, ii) PAA, iii) 4-CP and iv) 2, 4-D.

Fig. 11. Electrochemical impedance spectra of: i) $KClO_4$, ii) PAA, iii) 4-CP and iv) 2, 4-D with ZT-5 composite. Symbols represent the experimental data and continuous line represent the fitting to a $R_S(R_{CT}C_{dl})$ electric equivalent circuit.

Scheme. 1. Energy scheme of ZT-x composites and their interaction for spatial separation of photogenerated charge carriers.

Figures
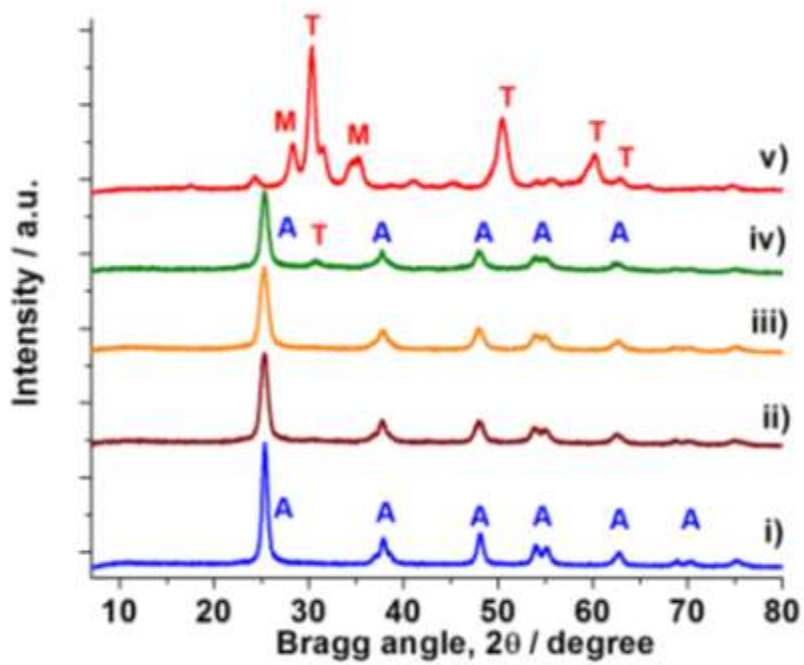
FIG. 1
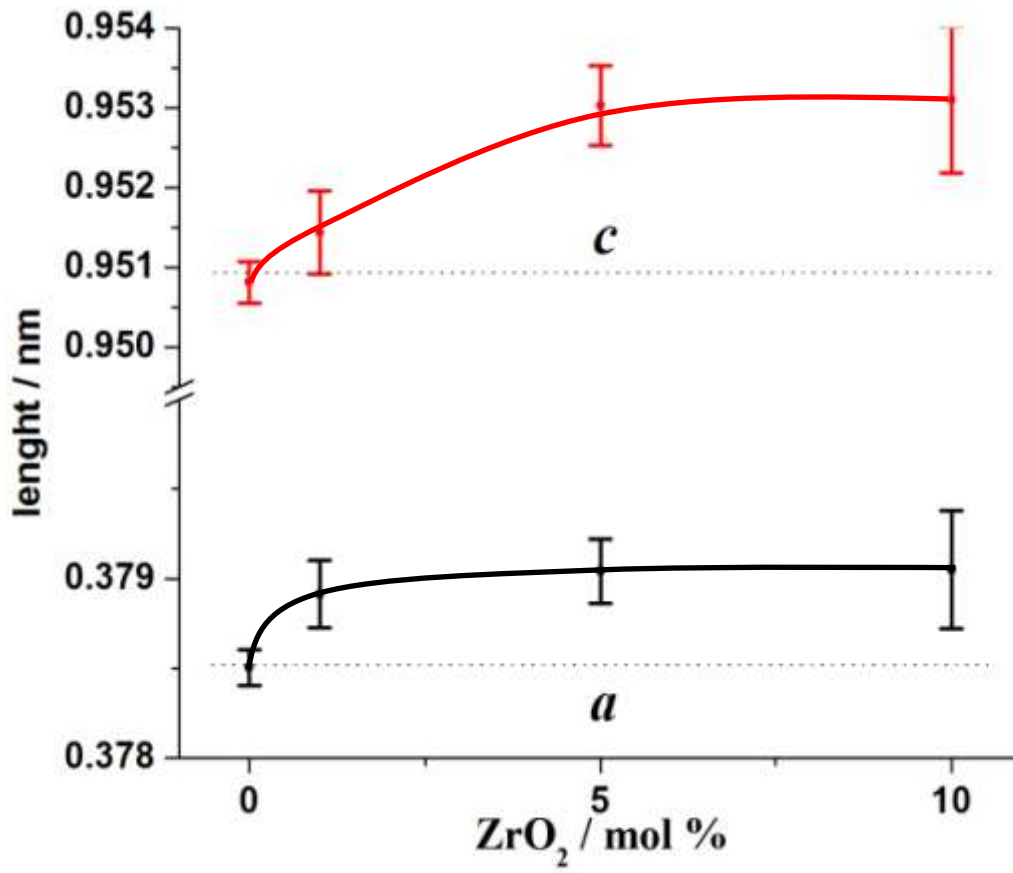
FIG. 2
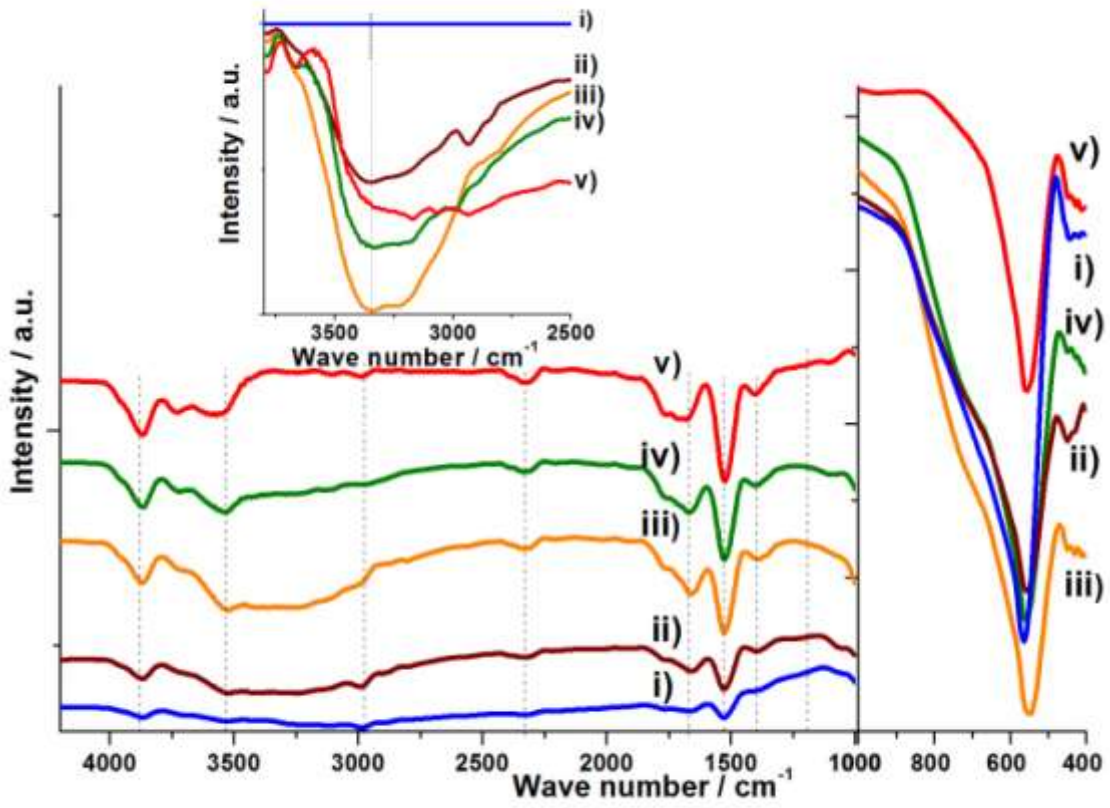
FIG. 3
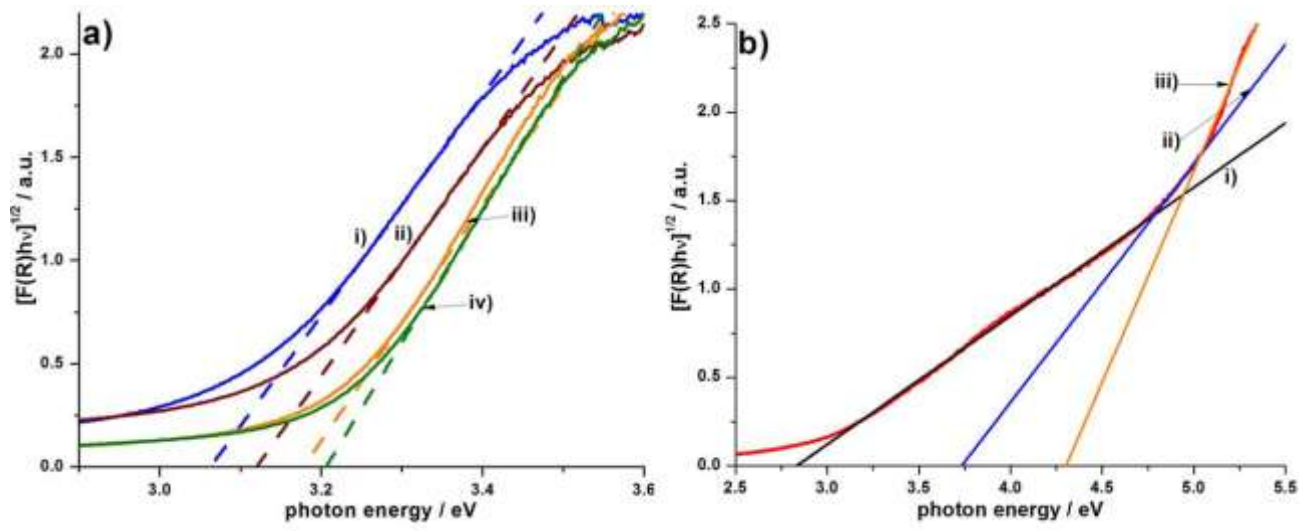
FIG. 4
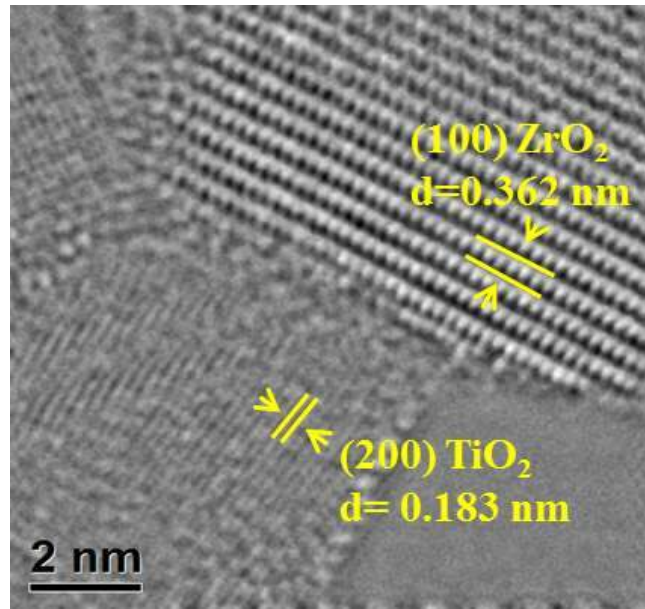
FIG. 5
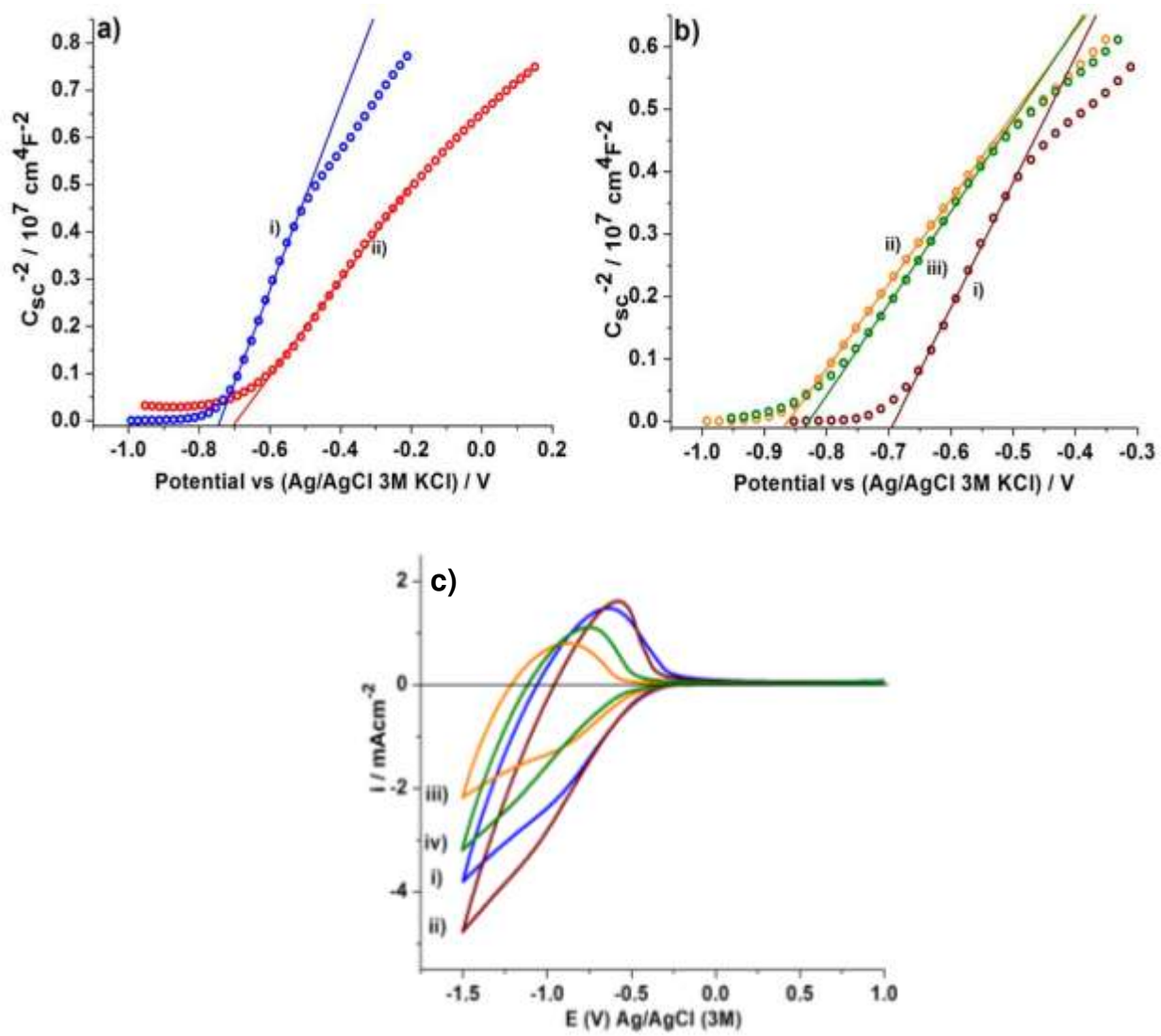
FIG. 6
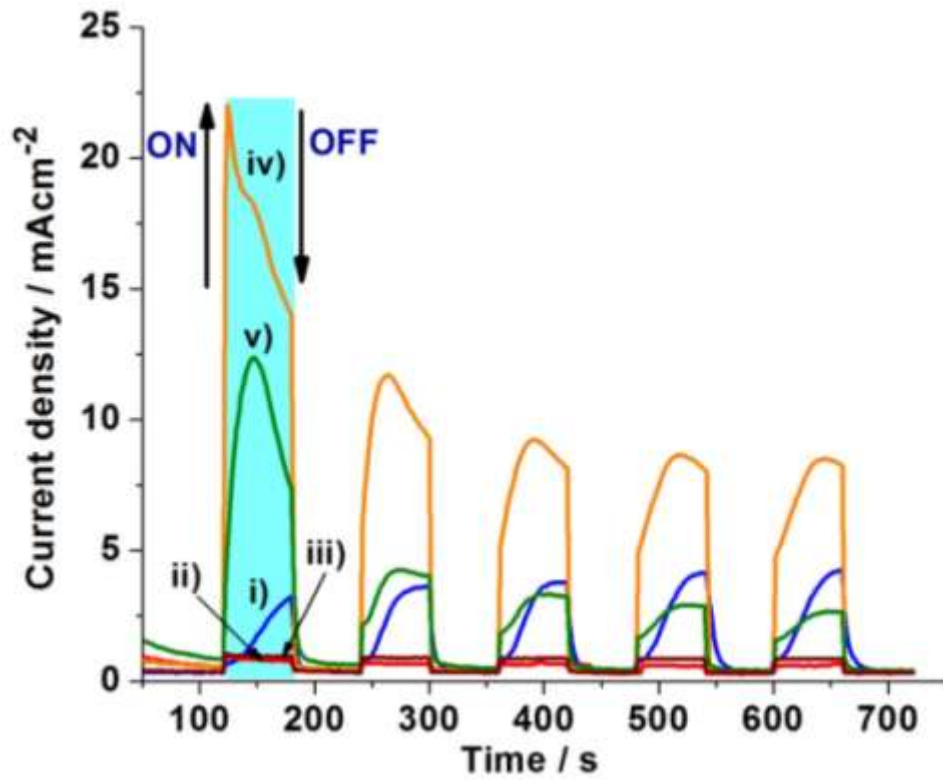
**FIG. 7**
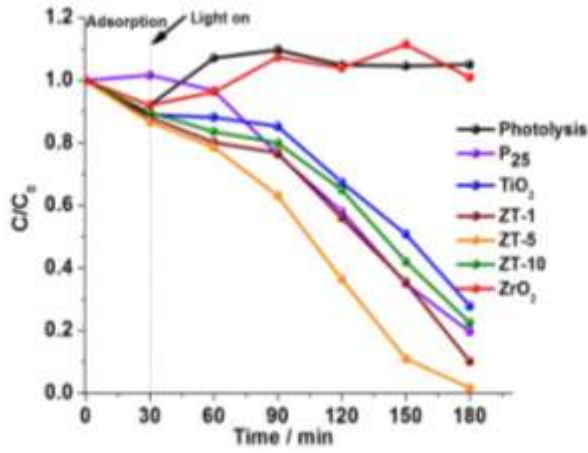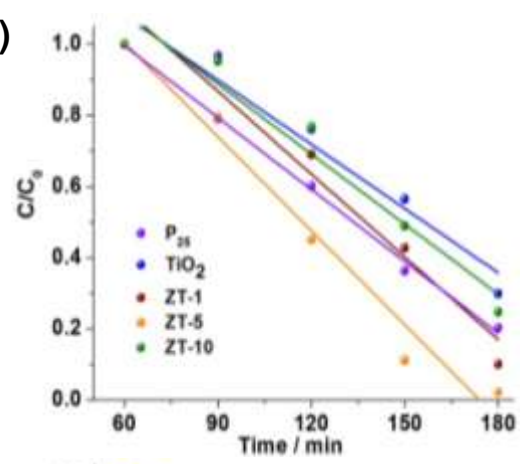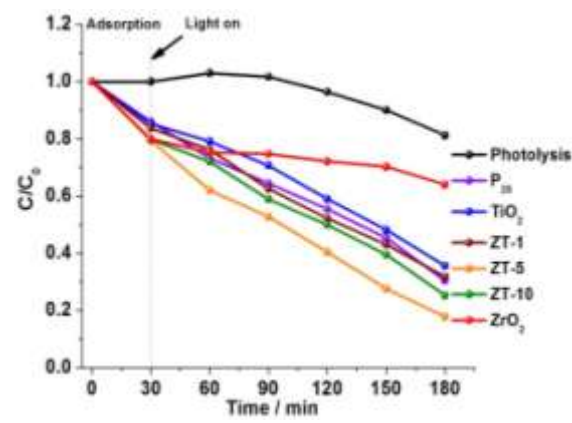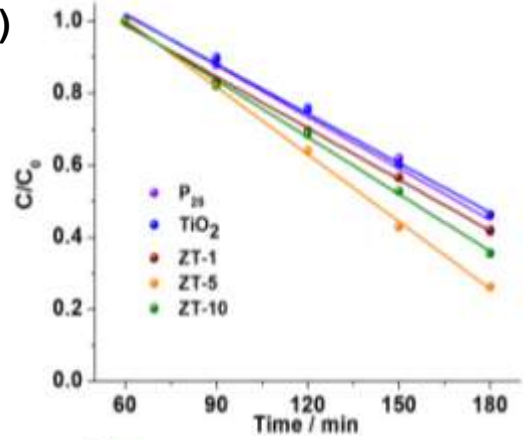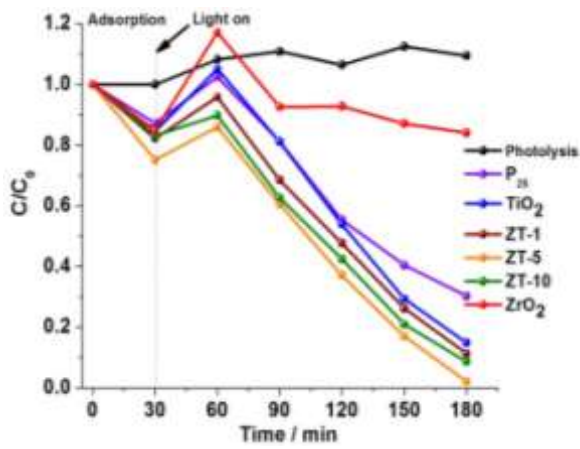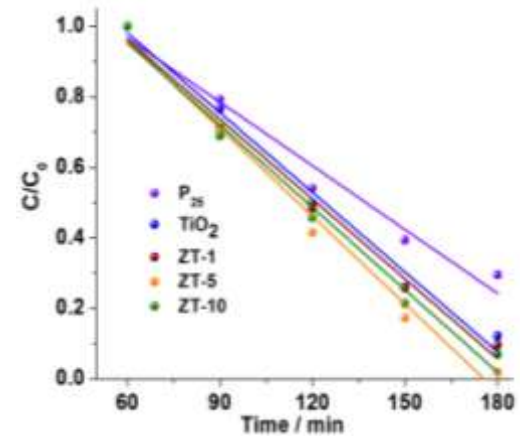
FIG. 8
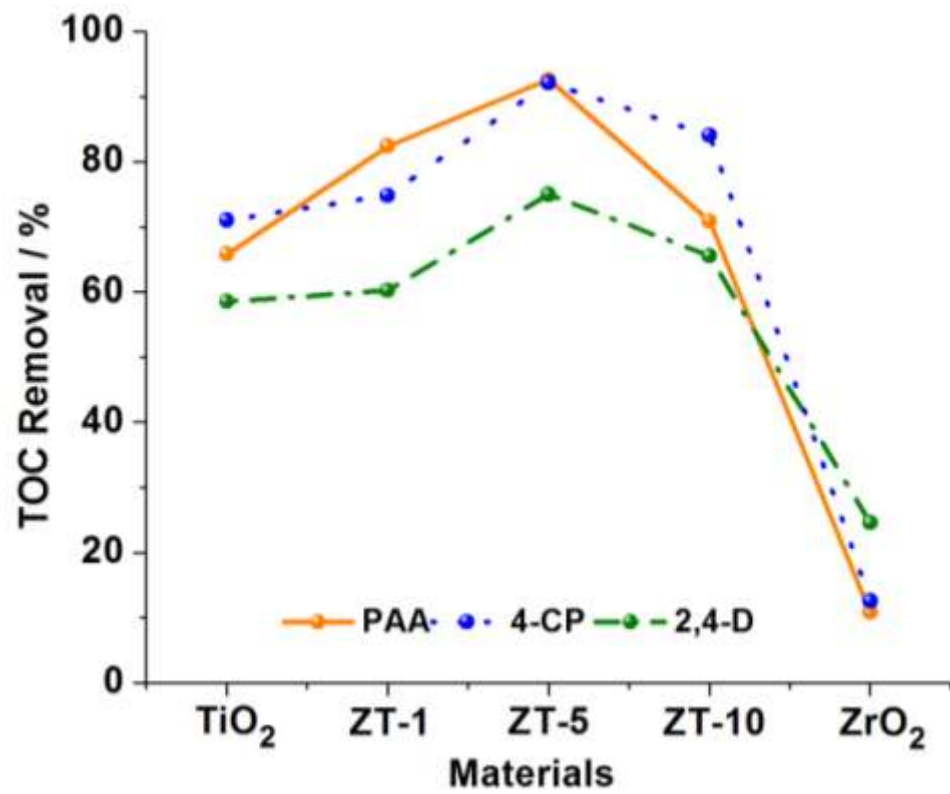
FIG. 9
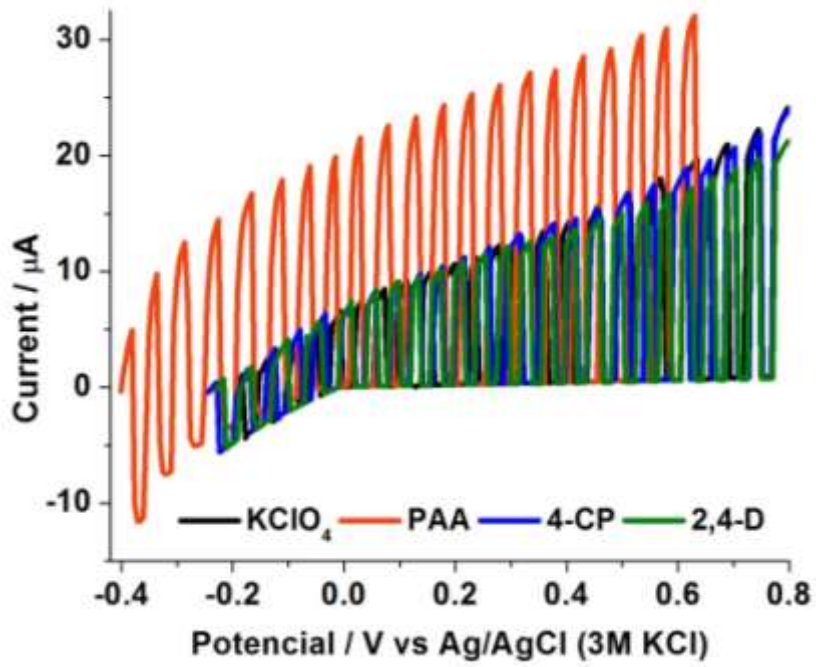
FIG. 10
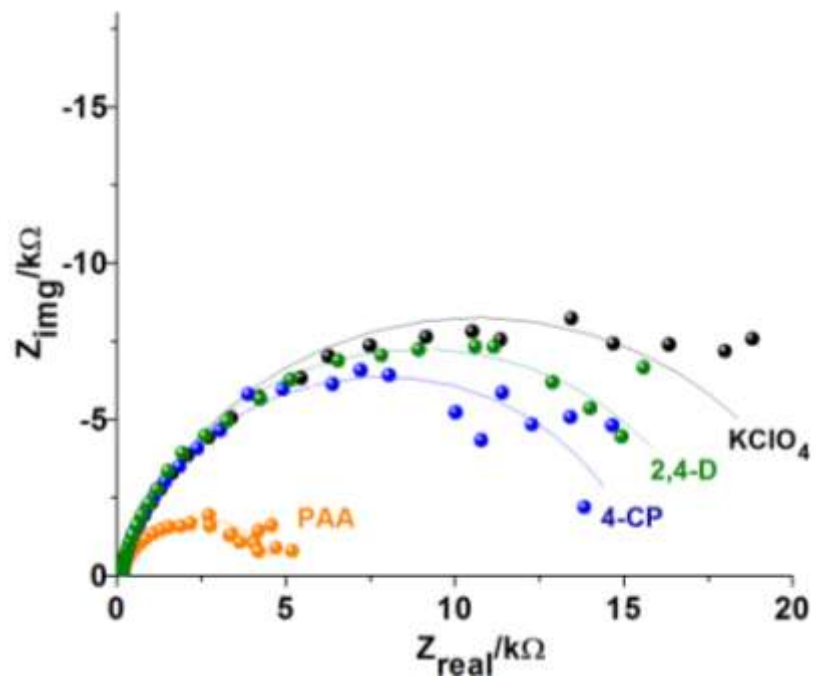
FIG. 11
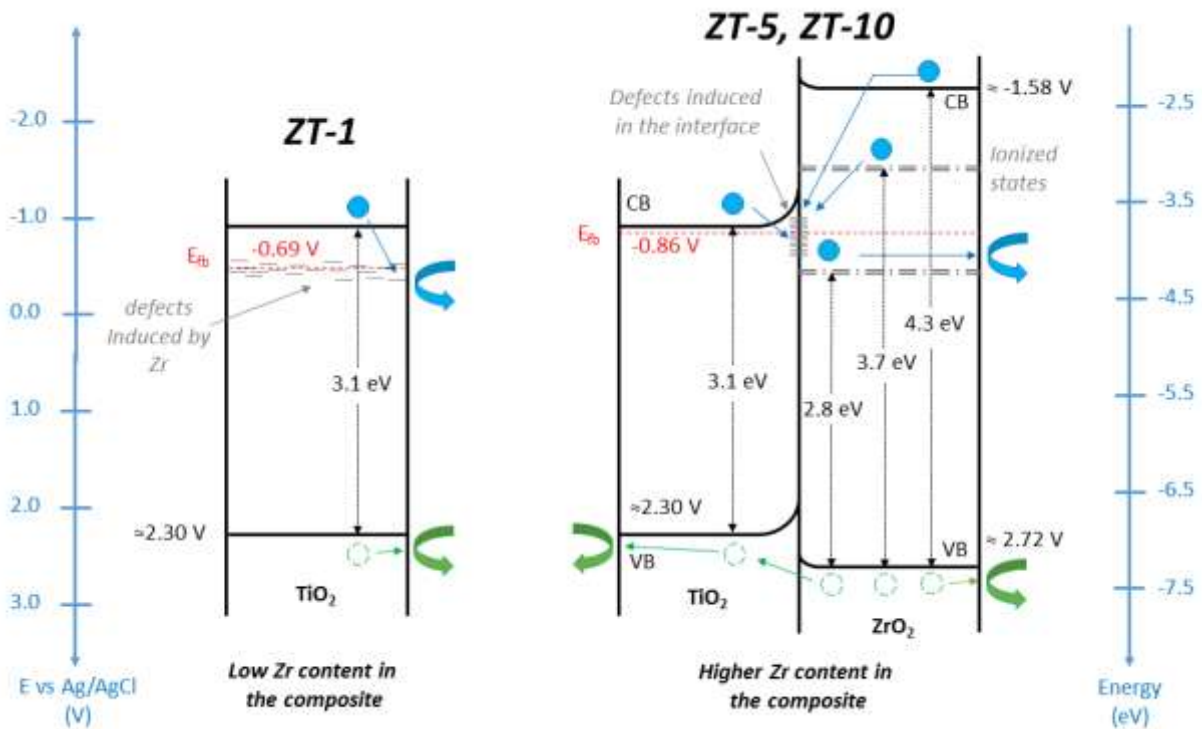
Scheme. 1.

Table Captions

Table 1. Structural, textural and optical properties of the calcined materials.

Table 2. The flat band potential (E_{fb}) and donor density (N_d) for calcined materials.

Table 3. Rate constants of zero order R^2 in the degradation of PAA, 4-CP and 2,4- D for the calcined materials.

Table 4. Parameters determined by Electrochemical Impedance Spectroscopy.

Tables

Table 1.

Materials	$D_{(101)-}$[*] nm	S_{BET}[‡] m^2/g	d_{pore}[‡] nm	V_{pore}[‡] cm^3/g	E_g[†] eV
TiO_2	12.7	51	2.4	0.08	3.1
ZT-1	7.8	146	6.5	0.32	3.1
ZT-5	8.8	147	7.8	0.37	3.2
ZT-10	9.1	142	9.6	0.46	3.2
ZrO_2	10.8	44	3.8	0.06	2.8 3.7 4.3

* Estimated from FWHM from the main peak in XRD patterns shown in Figure 1 using the Scherrer equation [28].

‡ Estimated by BET N_2 adsorption method.

† Estimated diffuse reflectance spectra Figure 3.

Table 2.

Material	E_{fb} vs (Ag/AgCl/ 3M KCl) (V)	N_d (10^{23}/ cm^3)
TiO$_2$	-0.740	0.834
ZT-1	-0.690	0.394
ZT-5	-0.862	1.012
ZT-10	-0.828	0.544
ZrO$_2$	-0.693	5.802

Table 3.

Materials	PAA		4-CP		2,4-D	
	k' $10^{-3}/min$	R^2	k' $10^{-3}/min$	R^2	k' $10^{-3}/min$	R^2
TiO$_2$	6.0	0.93	4.6	0.99	7.5	0.99
ZT1	7.8	0.94	4.8	1.0	7.5	0.99
ZT5	8.8	0.96	6.2	1.0	8.3	0.98
ZT10	6.6	0.94	5.3	1.0	7.8	0.98
P$_{25}$	6.7	0.99	4.7	0.98	6.0	0.96

Table 4.

Pollutant		R_{ct} ($k\Omega cm^2$)	C_{dl} (μFcm^{-2})	τ (s)
KClO$_4$	Off*	1423.9	31.8	45.30
	On	21.0	65.5	1.38
PAA		4.7	123.9	0.58
4-CP		15.4	69.6	1.07
2,4-D		17.7	77.0	1.36

*Not shown in Figure 9